Evaluation of Scatter Fraction and Count Rate Performance of Two Small-animal PET scanners using dedicated phantoms

Rameshwar Prasad, *Student Member, IEEE*, and Habib Zaidi, *Senior Member, IEEE*

***Abstract*– Positron Emission Tomography (PET) image quality deteriorates as the object size increases owing to increased detection of scattered and random events. The characterization of the scatter component in small animal PET imaging has received little attention owing to the small scatter fraction when imaging rodents. The purpose of this study is first to design and fabricate a dedicated cone-shaped phantom which can be used for measurement of object size dependent SF and noise equivalent count (NEC) rates and second, to evaluate those parameters for two small animal PET scanners, namely the X-PET™ and LabPET™-8 as function of radial offset, object size and lower energy threshold. Both scanners were modeled as realistically as possible using GATE Monte Carlo simulation platform. The simulation models were validated against experimental measurements in terms of sensitivity, SF and noise equivalent count rate (NECR). The dedicated phantom was designed and fabricated in-house using high-density polyethylene. The optimized dimensions of the cone-shaped phantom are 150 mm (length), 20 mm (minimum diameter), 70 mm (maximum diameter) and taper angle of 9°.The relative difference between simulated and experimental results for the LabPET™-8 scanner varied between 0.66% and 10% except for few results where it was below 16%. Depending on the radial offset from the axial centre for a central field of view (3-6 cm diameter), the SF for the cone-shaped phantom varied from 26.3 to 18.2% (X-PET™); 34.4 to 26.9% (LabPET™-8), 18.6 to 13.1% (X-PET™); 19.1 to 17.0% (LabPET™-8); 10.1 to 7.6% (X-PET™) and 9.1 to 7.3% (LabPET™-8) for lower energy thresholds of 250, 350 and 425 keV, respectively. The SF increases as the radial offset decreases, lower energy threshold (LET) decreases and object size increases. The SF values are higher for the LabPET™-8 compared to the X-PET™. The NECR increases as the radial offset increases and object size decreases. Maximum NECR was obtained at a LET of 350 keV for LabPET™-8 whereas 250 keV for X-PET™. High correlation coefficients (R^2) for SF and NECR were observed between the cone-shaped phantom and an equivalent volume cylindrical (EVC) phantom for the three considered axial fields-of-view. A single cone-shaped phantom enables the assessment of effects of three factors, namely radial offset, energy threshold and object size on small animal PET imaging characteristics like SF and NECR. Hence, a cone-shaped phantom may be more suited for evaluation of object size-dependent SF and NECR instead of using various discrete phantoms of different size.**

***Index Terms*—** PET, instrumentation, small animals, performance evaluation, NEMA.

I. INTRODUCTION

Positron emission tomography (PET), a non-invasive molecular imaging modality, is being widely used for qualitative characterization and quantification of biochemical processes in preclinical and pharmacological research. PET scanners dedicated to small-animal imaging provide high spatial resolution and high sensitivity that are vital to *in vivo* molecular imaging.[1] This steered the development of various design concepts and technologies for preclinical PET imaging.[2] The image quality and quantitative accuracy of PET images are degraded by a number of physical factors such as the attenuation of the photons being detected, the detection of scattered photons and the finite spatial resolution of the imaging system. Scattered events degrade both quality and quantitation of PET imaging. Scatter fraction is a useful parameter to access the magnitude of scatter and to estimate the potential impact of scatter on the reconstructed images. The SF is a vital component of the NECR estimation.[3] NECR is an important measure of image quality in the PET imaging. The SF largely depends on the object size and density, energy window settings, the photon energy and the tomograph geometry (acquisition mode 2D or 3D). The SF is well accessed and documented for clinical PET imaging. This represents 10% to 20% in the 2D mode, whereas in the 3D mode it is 30% to 35% in brain imaging and 50% to 60% in whole-body PET imaging.[4, 5] Though the characterization of the scatter component in small animal PET imaging has received little attention owing to the small scatter fraction, some SF values have been reported for several different small animal scanners. These are 5%-20% for mouse imaging whereas 15%-30% are reported for rat imaging.[6-12] The scatter fraction (SF) and NECR measurements are usually measured using various discrete phantoms of different uniform size. The National Electrical Manufacturers Association (NEMA)-04 standards [13] suggests three different phantoms of 25 mm, 50 mm, and 100 mm diameter for mouse, rat and monkey sized phantoms, respectively, for SF and count rate measurements of small animal PET scanners. Moreover, it has been suggested that a phantom representing a varying range of cross-sections and dimensions would be more suited for the assessment of these parameters for clinical PET systems.[14]

The purpose of this study is first to design and develop a dedicated cone-shaped phantom which can be used for measuring object size dependent SF and NECR and, second, to assess these parameters as function of radial offset, object size and lower energy threshold for two small animal PET scanners, namely the X-PET™ and LabPET™-8 using this cone-shaped phantom.

This work was supported by the Swiss National Foundation under grant No. 3152A0-102143.

Rameshwar Prasad is with Division of Nuclear Medicine and Molecular Imaging, Geneva University Hospital, CH-1211 Geneva, Switzerland (e-mail: rameshwar.prasad@unige.ch)

Habib Zaidi is with the Division of Nuclear Medicine and Molecular Imaging, Geneva University Hospital CH-1211 Geneva, Switzerland and Department of Nuclear Medicine and Molecular Imaging, University Medical Center, Gronigen, University of Groningen, 9700 RB Groningen, Netherlands (e-mail: habib.zaidi@hcuge.ch).

II. Materials and Methods

A. Monte Carlo modeling of small animal PET scanners

Two small animal PET scanners namely, X-PET™ and LabPET™-8 have been accessed. Both of these scanners are commercialized by GE healthcare Technologies (Waukesha, WI). The X-PET™ is a dedicated $Bi_4Ge_3O_{12}$ (BGO)-based small animal PET scanner having 11.6 cm axial FOV and incorporating various technological innovations to improve system performance.[7] For instance, the photomultiplier-quadrant-sharing (PQS) method is used to maximize the number of crystals per photomultiplier whereas a high-yield pileup event recovery (HYPER) electronic processing technology is exploited to improve the count-rate performance.[15] On the other hand, the LabPET™-8 is an APD-based digital PET scanner having 7.5 cm axial FOV, designed with quasi-individual crystal readout along with parallel digital architecture to achieve high-performance.[16] Scintillation crystals composed of $Lu_{0.4}Gd_{1.6}SiO_5$ (LGSO) and $Lu_{1.9}Y_{0.1}SiO_5$ (LYSO) are optically coupled one after the other, forming phoswich pairs of detectors and read out by a single APD.[16] Some important features of both scanners are summarized in Table 1.

Both the X-PET™ and LabPET™-8 scanners were modeled as realistically as possible in terms of geometry, physics of photon transport and signal processing using the GATE Monte Carlo simulation toolkit.[17] GATE is a dedicated Monte Carlo software package for emission tomography. This software allows for modelling detailed scanner geometries and radiation interactions with matter, tracking events (recording position, time and energy of an event), and creating various types of output files including projection and ASCII files. This package is based on the well-established Geant4 libraries[18] featuring a modular, versatile, scripted simulation toolkit**.** Geant4 is a toolkit for the simulation of the physics of propagation and interaction of particles through matter.

For the X-PET™, pentagonal detector blocks were modeled using trapezoidal volumes in GATE. An energy resolution of 25% for 511 keV photons was applied as blurring kernel for energies deposited within the crystals[19]. The lower energy threshold was set to 250 keV whereas the higher energy threshold was set to 750 keV in all simulations for the X-PET™ scanner. These energy thresholds were chosen based on default energy thresholds available on real X-PET™ scanner.

For the LabPET™-8, the GATE materials database was modified to add LYSO, LGSO and kovar. For both LYSO and LGSO, an energy resolution of 25% and an average timing resolution of 9 ns were set. The coincidence window was set to 20 ns .The lower energy threshold was set to 250 keV whereas the higher energy threshold was set to 650 keV. These energy thresholds and coincidence window settings were chosen to match the settings available on real LabPET™-8 scanner.

For both scanners, back-to-back 511 keV annihilation photons were generated to decrease the computation time. The animal positioning bed was not modeled for both scanners. The GATE output information was recorded in ASCII format and then rebinned into sinograms using single-slice rebinning (SSRB) as required for NEMA-04 analysis of SF and count rate performance.

The data were processed using programs developed in-house implemented in MATLAB 7.4 (Mathworks, Natick, MA). The X-PET™ simulation model was validated against experimental result[7] whereas the LabPET™-8 simulation model was validated against experimental results performed by our group and those reported by Bergeron *et al.*[20] in terms of sensitivity, noise equivalent count rate (NECR), and SF for mouse and rat-sized phantoms.

Table 1. Summary of technical specifications of the X-PET™ and LabPET™-8 preclinical PET scanners.

Type	X-PET™	LabPET™-8
Scintillator	BGO	LYSO+LGSO
Crystal dimension	2.32×2.32×9.4 mm^3	2.0×2.0×14 mm^3
No. of detector rings	48	32
Crystals per ring	240	192
Total no. of crystals	11520	6144
Detector ring inner diameter	165 mm	162 mm
Transaxial field-of-view	100 mm	100 mm
Axial field-of-view	116 mm	75 mm
Image pixel size (mm)	0.4	0.5
Slice thickness (mm)	0.4	0.25/0.5

B. Design and fabrication of the cone-shape phantom

The parameters considered for phantom design are material, cross-sectional dimensions and taper angle (θ). The taper angle (θ) is described in Fig. 1. The fabrication material chosen is high density polyethylene (density of 0.96±0.1 g/cm^3) as prescribed in the NEMA-NU04 standards for SF and count rate measurements. The maximum diameter of phantom was derived from the transaxial FOV of various small animal scanners [6, 7, 21] respectively. Based on this assessment, the maximum diameter of the phantom was set to 70 mm by considering 70% of the average maximum diameter of the transaxial FOV. The minimum diameter of the phantom was set 2 cm because of fabricating milling machine limitation. The length of phantom depends on the taper angle. As θ increases, the phantom length decreases but in this case the range of the cross-sectional volume in a single PET axial FOV increases, making it less representative of an equivalent volume cylindrical (EVC) phantom and hence results can vary for fully three-dimensional (3D) PET imaging. However, when θ becomes smaller, this makes phantom long enough for the small-animal PET axial FOV. Here, the EVC phantom is defined as a phantom having uniform cylindrical shape and diameter equal to the diameter of the cone-shaped phantom in the middle of the axial FOV of scanner. When $\theta = 0^o$, the

cone-shape phantom corresponds to EVC phantom having diameter of maximum or minimum side of cone-shaped phantom. Thus, optimization of taper angle becomes crucial in designing of cone-shaped phantom. Different cone-shaped phantoms with minimum diameter 2 cm, maximum diameter 7 cm, and taper angles of 5°, 7°, 9°, and 11° were simulated using Monte Carlo simulation model for X-PET™ scanner as discussed in section 2.1. Line source of different lengths having back-to-back 511 keV annihilation photons was placed in centre of phantom. Simulated data were acquired for different taper angles of 5°, 7°, 9°, and 11° and its corresponding EVC phantom having diameter 5.5 cm, 5cm, 4.5 cm and 4 cm respectively. The taper angle was optimized by analyzing the simulated data of the X-PET™ scanner in terms of SF, NECR, true count rates using the NEMA-NU04 standards.

The phantom was fabricated in-house considering the optimized design considerations including material, cross-sectional dimensions and taper angle. To study the effects of radial offsets four holes (diameter 4 mm) were drilled parallel to the long axis at the centre and at radial offset positions of 10, 15 and 20 mm. Solid line fillings of the same material used for the phantom were also fabricated. The different FOVs of cone-shaped phantom which corresponds to minimum, middle and maximum diameter region in the scanner's axial FOV are named as FOVmouse, FOVrat, and FOVrabbit respectively. Depending on scanner axial FOV the cone-shaped phantom can be exploited to simulate the various sizes of mouse, rats and small rabbits used in small animal PET imaging.

C. *Studies using cone-shaped phantom*

The optimized cone-shaped phantom was further used to access the magnitude of scatter and NECR as function of varying phantom size, lower energy thresholds, and line source positions for two small animal PET scanners using simulation and experimental studies.

PET data were simulated and analyzed for a line source at the centre and at radial offsets of 10, 15 and 20 mm for lower energy thresholds (LETs) of 250, 350 and 425 keV, whereas the higher energy threshold was kept constant (650 keV for LabPET™-8 and 750 keV for the X-PET™). Back-to-back 511 keV annihilation photons were simulated for the one line source at a time (10^9 events). All simulations were performed at a low radioactivity regime as defined in the NEMA-04 standards for SF calculation. Data were collected at 3 different axial FOVs from one end to the other end of the phantom in 3 successive axial steps, namely FOVmouse, FOVrat, and FOVrabbit. An EVC of the cone-shaped phantom at three different axial FOVs was also considered.

The experimental studies were done using the LabPET™-8 scanner. The line source was filled with 2 MBq of ^{18}F and inserted in the central hole of the phantom while the other holes were closed using the fillings. The data were acquired for all 3 FOVs one after the other. This was repeated for other holes. Each acquisition lasted 5 minutes. PET studies were acquired using a default energy window of 250–650 keV and 22 ns coincidence timing window in list-mode format which were binned into 3D sinograms. These 3D sinograms were further rebinned to two-dimensional (2D) sinograms using SSRB. These 2D sinograms were used for further analysis adhering to NEMA-NU04 standards. The relative difference (%) between simulated and experimental results was also calculated.

III. RESULTS

A. *Validation of GATE*

Fig. 1a illustrates the modeled LabPET™-8 scanner using GATE toolkit. The validation results of simulated models of X-PET™ and LabPET™-8 scanner are presented in Table 2. It can be seen that the relative difference between simulated and measured values varied from 4.8 % to 10.8 % for all parameters considered, rendering these simulated scanners accurate for further PET data acquisitions.

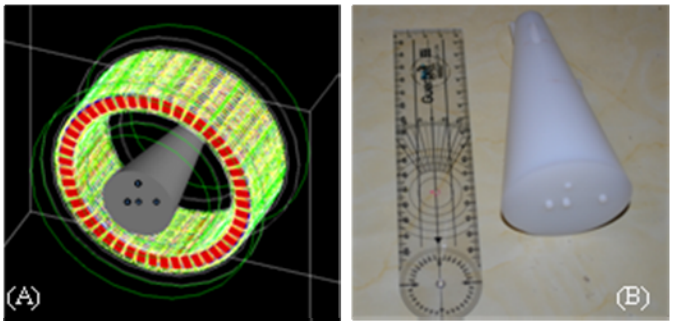

Fig. 1. (A) Simulation model of the LabPET™-8 scanner using GATE. (B) Photograph of the fabricated cone-shaped physical phantom.

B. *Cone-shaped phantom*

The developed physical cone-shaped phantom is shown in Fig. 1b. The optimized minimum and maximum diameter of cone-shaped phantom are 2 cm and 7 cm respectively. Out of four simulated taper angles, an angle of 11° produced the highest total, true and NECR events rate whereas it resulted in the lowest SF. Figure 2 presents the SF profile for slice numbers covering the axial FOV of X-PET™ scanner. It can be observed that the SF profiles for 9° and 11° are closer to the SF profile of the EVC phantom. Since a maximum taper angle of 10° was possible for the milling machine available in the workshop used to fabricate the phantom, a taper angle of 9° was chosen. Based on taper angle of 9° the length of phantom was chosen as 15 cm.

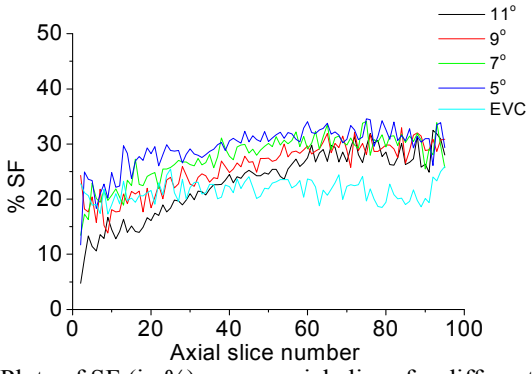

Fig. 2. Plots of SF (in %) versus axial slices for different taper angles for the cone-shaped phantom and equivalent cylindrical volume (EVC) phantom.

Table 2. Comparison between simulated and measured performance parameters of the X-PET™ and LabPET™-8 small animal PET scanners.

	X-PET™			LabPET™-8		
Parameter	Simulated	Measured	Rel. Err. (%)	Simulated	Measured	Rel. Err. (%)
SF(%) mouse phantom	7.2	7.9	9.2	18.10	19	4.8
SF(%) rat phantom	19.1	21	9.4	28.18	31	9.5
Peak NECR (kcps) mouse phantom	114	106	7.2	204	183	10.8
Absolute Sensitivity (%)	6.3	5.9	6.5	1.46	1.33	9.3

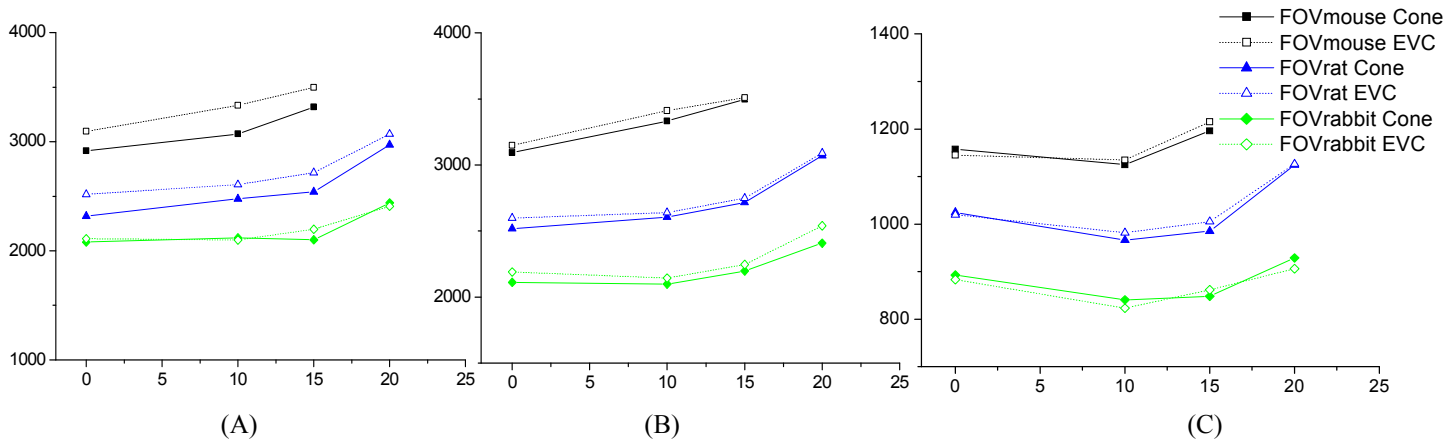

Fig. 3. Trends of the LabPET™-8 NECR as function of radial offsets for the cone-shaped and EVC phantoms using different LETs: (A) 250 keV, (B) 350 keV (C) 425 keV.

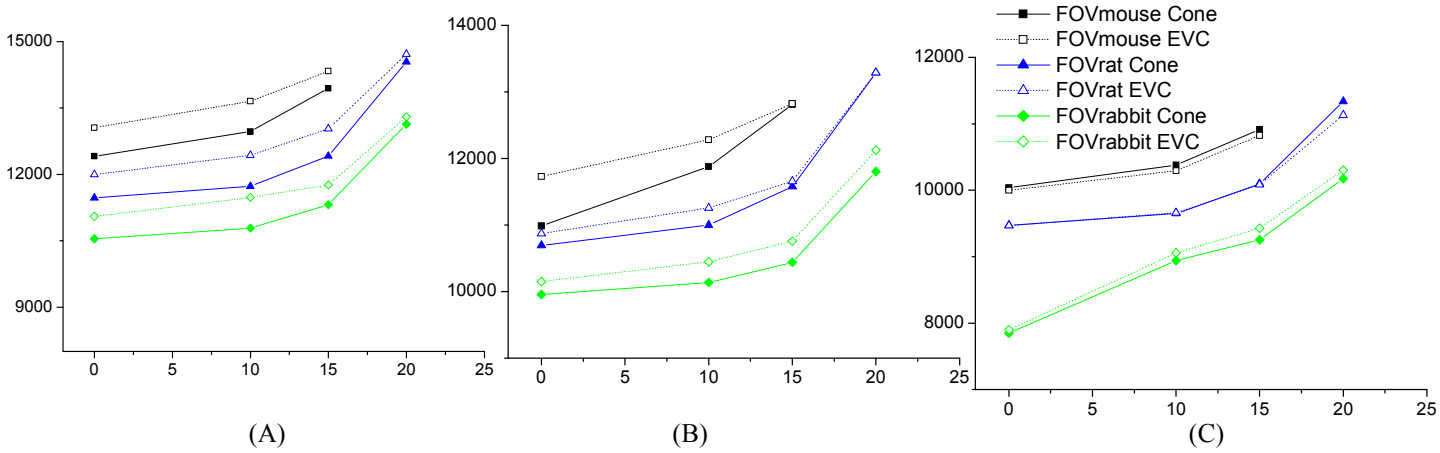

Fig. 4. Trends of the X-PET™ scanner NECR as function of radial offsets for the cone-shaped and EVC phantoms using different LETs: (A) 250 keV, (B) 350 keV (C) 425 keV.

Table 3. Correlation coefficient (R^2) for NECR and SF between the cone-shaped phantom and EVC phantom for both the X-PET™ and LabPET™-8 scanners.

Scanner	LET	FOV_{mouse}		FOV_{rat}		FOV_{rabbit}	
		SF	NECR	SF	NECR	SF	NECR
X-PET™	250	0.990	0.999	0.998	0.996	0.992	0.995
	350	0.950	0.999	0.996	0.999	0.982	0.998
	425	0.965	0.999	0.895	0.996	0.951	0.960
LabPET™-8	250	0.963	0.973	0.999	0.995	0.885	0.946
	350	0.958	0.988	0.932	0.997	0.954	0.993
	425	0.990	0.999	0.983	0.990	0.988	0.923

C. *Studies using cone-shaped phantom*

Using cone-shaped phantom, the SF for the FOVrat varied as a function of the line source's radial offset from 26.3 to 18.2% (X-PET™) and 34.4 to 26.9% (LabPET™-8), 18.6 to 13.1% (X-PET™) and 19.1 to 17.0% (LabPET™-8), and 10.1 to 7.6% (X-PET™) and 9.14 to 7.3% (LabPET™-8) for LETs of 250, 350 and 425 keV, respectively. For EVC, these varied as 21.84 to 15.49 % (X-PET™) and 29.84 to 23.83 % (LabPET™-8), 16.98 to 11.34% (X-PET™) and 18.61 to 14.39 % (LabPET™-8), and 10.68 to 7.55 % (X-PET™) and 9.13 to 6.97 % (LabPET™-8) for LETs of 250, 350 and 425 keV, respectively.

Fig. 3 shows plots of the NECR for the LabPET™-8 scanner for both the cone-shaped and EVC phantoms for 3 axial FOVs versus the line source radial offset for a LETs of 250, 350 and 425 keV. Similar quantities are plotted for X-PET™ scanner in Fig. 4. Table 3 highlights high correlation coefficients (R^2) of SF and NECR between the cone-shaped phantom and the EVC phantom for different accessed axial FOVs using X-PET™ and LabPET™-8 scanner.

The SF for both the scanners decreased as the radial offset increased, lower energy threshold increased and object size decreased. However, in all cases the SF of LabPET™-8 is higher than X-PET™ scanner. The NECR for both the scanners increased as the radial offset increased, object size decreased. The maximum NECR was for LabPET™-8 at LET of 350 keV whereas it was maximum at LET of 250 keV for the X-PET™. However, in all cases the NECR of X-PET™ is higher than LabPET™-8 scanner.

The experimental studies using cone-shaped phantom have been acquired using LabPET™-8 scanner. Figure 5 shows the percent relative difference between simulated and experimental results for the LabPET™-8 scanner in terms of NECR and SF as function of line source radial position for the various FOVs considered (FOVmouse, FOVrat, and FOVrabbit). The results, obtained using an energy window of 250-650 keV, varied mostly between 0.66% and 10%, and remain overall below 16%.

IV. DISCUSSION

The SF and NECR are important parameters for optimization of acquisition protocol settings such as timing and energy windows, and evaluating the image quality of different small animal PET scanners. Additionally, SF useful in determination of the level of scatter correction required for a small animal PET study. These parameters are usually measured using various discrete and uniform phantoms of different size. Moreover, within a particular rodents' species especially rat or small rabbits there is variation in body size. Hence, a single cone-shaped phantom which would be suitable for object size-dependent small animal PET system SF and NECR assessment was designed and fabricated. The phantom was optimized using Monte Carlo simulated models of the LabPET™-8 and X-PET™ scanners using the GATE toolkit. The validation of simulation models against experimental measurements proved that the models are capable of predicting the response of real systems within acceptable limits. For all considered validation parameters of two scanners, the difference between simulated and experimental results varied between 4.8% and 10.8%. The methodology

followed for the design and optimization of the cone-shaped phantom is an extension of the work described by Wilson *et al.*[14] to small animal PET imaging. The phantom described in the reference above is a fillable tapered design suitable for clinical imaging, whereas we opted for a solid tapered phantom dedicated for small animal PET imaging having multiple holes to insert line sources at different radial offset positions. Using the cone-shaped phantom, the difference between simulated and experimental SF and NECR results for the LabPET™-8 scanner is below 16%. It should be noted that we have not considered the animal bed, the intrinsic radioactivity from LGSO and LYSO crystals in simulation model.

The SF decreases as the radial offset increases from centre to radial offset of 20 mm, lower energy threshold increases from 250 to 425 keV and, object size decreases from small rabbit body size to mouse body size. The NECR for both the scanners increased as the radial offset increased, object size decreased. The maximum NECR for LabPET™-8 is at LET of 350 keV whereas it is at LET of 250 keV for X-PET™. This presents the effect radial position, object size and LET on SF and NECR which in turn affects the image quality of small animal PET imaging. Similar behavior have been reported in ref.[22] The SF for the LabPET™-8 is higher than for the X-PET™ when using the same settings. This can be attributed due to the detector housing and FOV shielding of the LabPET™ scanner which in turn increases the signal detection efficiency by 23%,[23] the higher out-of-FOV radioactivity for the LabPET™-8 owing to shorter axial FOV, inter-crystal scattering which is higher for LSO compared to BGO and the inherent scintillation crystal material characteristics. Moreover, the difference between SF of LabPET™-8 and X-PET™ decreases as the lower energy threshold increases. An interesting aspect of the cone-shaped phantom is that it allowed the assessment of the effect of three parameters, namely radial offset, energy threshold and object size in single phantom acquisition. The FOVmouse, FOVrat, and FOVrabbit region in cone-shape phantom can be used for accessing the SF and NECR for various sizes of mouse, rats and small rabbits respectively.

High correlation coefficients for SF and NECR were observed between the cone-shaped phantom and the EVC phantom for different axial FOVs. This shows that the cone-shaped phantom may be suitable than the uniform EVC phantom. Similar conclusions were drawn by Wilson *et al.*[14]

V. CONCLUSION

A dedicated cone-shaped phantom was designed and fabricated for measuring object size-dependent SF and NECR for small animal PET scanners. The effect of varying radial offset, object size and lower energy threshold on SF and NECR was evaluated for two small animal PET scanners, namely the X-PET™ and LabPET™-8 using this phantom through Monte Carlo simulations and experimental studies. A single cone-shaped phantom provides the feasibility of assessing the effect of three factors, namely radial offset, energy threshold and object size on the parameters like SF and NECR for various sizes of mouse, rats and small rabbits.

ACKNOWLEDGEMENTS

This work was supported by the Swiss National Science Foundation under grant SNSF 3152A0-102143. The authors would like to thank Jean-Daniel Leroux and Roger Lecomte from the University of Sherbrooke, Canada, for their help with Monte Carlo modeling of the LabPET™ system.

REFERENCES

[1] A. F. Chatziioannou, "Molecular imaging of small animals with dedicated PET tomographs.," *Eur J Nucl Med Mol Imaging,* vol. 29, pp. 98-114, Jan 2002.

[2] C. S. Levin and H. Zaidi, "Current trends in preclinical PET system design.," *PET Clinics,* vol. 2, pp. 125-160, 2007/4 2007.

[3] S. C. Strother, M. E. Casey, and E. J. Hoffman, "Measuring PET scanner sensitivity: relating countrates to image signal-to-noise ratios using noise equivalents counts," *IEEE Trans Nucl Sci,* vol. 37, pp. 783-788, 1990.

[4] H. Zaidi and K. F. Koral, "Scatter modelling and compensation in emission tomography.," *Eur J Nucl Med Mol Imaging,* vol. 31, pp. 761-782, 2004.

[5] H. Zaidi and M.-L. Montandon, "Scatter compensation techniques in PET.," *PET Clinics,* vol. 2, pp. 219-234, 2007/4 2007.

[6] Q. Bao, D. Newport, M. Chen, D. B. Stout, and A. F. Chatziioannou, "Performance evaluation of the Inveon dedicated PET preclinical tomograph based on the NEMA NU-4 standards.," *J Nucl Med,* vol. 50, pp. 401-408, March 1, 2009 2009.

[7] R. Prasad, O. Ratib, and H. Zaidi, "Performance evaluation of the FLEX Triumph™ X-PET scanner using the NEMA NU-04 standards," *J Nucl Med* vol. 51, pp. 1608-15, 2010.

[8] Y. C. Tai, A. Ruangma, D. Rowland, S. Siegel, D. F. Newport, P. L. Chow, and R. Laforest, "Performance evaluation of the microPET focus: a third-generation microPET scanner dedicated to animal imaging.," *J Nucl Med,* vol. 46, pp. 455-463, Mar 2005.

[9] J. S. Kim, J. S. Lee, K. C. Im, S. J. Kim, S.-Y. Kim, D. S. Lee, and D. H. Moon, "Performance measurement of the microPET Focus 120 scanner.," *J Nucl Med,* vol. 48, pp. 1527-1535, September 1, 2007 2007.

[10] A. Del Guerra, A. Bartoli, N. Belcari, D. Herbert, A. Motta, A. Vaiano, G. Di Domenico, N. Sabba, E. Moretti, G. Zavattini, M. Lazzarotti, L. Sensi, M. Larobina, and L. Uccelli, "Performance evaluation of the fully engineered YAP-(S)PET scanner for small animal imaging.," *IEEE Trans Nucl Sci,* vol. 53, pp. 1078-1083, 2006.

[11] M. C. Bergeron, J.; Bureau-Oxton, C.; Beaudoin, J.-F.; Tetrault, M.-A.; Leroux, J.-D.; Lepage, M.D.; Robert, G.; Fontaine, R.; Lecomte, R.; , "Performance evaluation of the LabPET12, a large axial FOV APD-based digital PET scanner " *Nuclear Science Symposium Conference Record (NSS/MIC), 2009 IEEE* pp. 4017-4021, 2009.

[12] R. Prasad, O. Ratib, and H. Zaidi, "NEMA NU-04-based performance characteristics of the LabPET-8™ small animal PET scanner," *Phys. Med. Biol.,* vol. 56, pp. 6649–6664, 2011.

[13] National Electrical Manufacturers Association, "NEMA Standards Publication NU 4 – 2008. Performance Measurements of Small Animal Positron Emission Tomographs," National Electrical Manufacturers Association, Rosslyn, VA 2008.

[14] J. M. Wilson, S. J. Lokitz, and T. G. Turkington, "Development of a fillable, tapered PET/CT phantom.," *IEEE Trans Nuc Sci,* vol. 58, pp. 651-659, 2011.

[15] W.-H. Wong, H. Li, J. Uribe, H. Baghaei, Y. Wang, and S. Yokoyama, "Feasibility of a high-speed gamma-camera design using the high-yield-pileup-event-recovery method.," *J Nucl Med,* vol. 42, pp. 624-632, April 1, 2001 2001.

[16] M. Bergeron, J. Cadorette, J. F. Beaudoin, M. D. Lepage, G. Robert, V. Selivanov, M. A. Tetrault, N. Viscogliosi, J. P. Norenberg, R. Fontaine, and R. Lecomte, "Performance evaluation of the LabPET APD-based digital PET scanner.," *IEEE Trans Nucl Sci,* vol. 56, pp. 10-16, 2009.

[17] S. Jan, G. Santin, D. Strul, et al, "GATE: a simulation toolkit for PET and SPECT.," *Phys Med Biol,* vol. 49, pp. 4543-4561, 2004.

[18] S. Agostinelli, J. Allison, K. Amako, J. Apostolakis, H. Araujo, P. Arce, M. Asai, D. Axen, S. Banerjee, and G. U. Barrand, "GEANT4- a simulation toolkit.," *Nucl Instrum Methods A,* vol. 506, pp. 250-303, 7/1 2003.

[19] N. Zeraatkar, M. R. Ay, A. R. Kamali-Asl, and H. Zaidi, "Accurate Monte Carlo modeling and performance assessment of the X-PET subsystem of the FLEX Triumph[sup [trademark sign]] preclinical PET/CT scanner.," *Med Phys,* vol. 38, pp. 1217-1225, 2011.

[20] M. Bergeron, J. Cadorette, J.-F. Beaudoin, M.-A. Tetrault, N. Viscogliosi, V. Selivanov, M. D. Lepage, G. Robert, J. P. Norenberg, R. Fontaine, and R. Lecomte, "Imaging performance of the LabPET™ APD-based digital PET scanner," in *IEEE Nuclear Science Symposium Conference Record*, 2008, pp. 3841-3845.

[21] Y. Wang, J. Seidel, B. M. Tsui, J. J. Vaquero, and M. G. Pomper, "Performance evaluation of the GE Healthcare eXplore VISTA dual-ring small-animal PET scanner.," *J Nucl Med,* vol. 47, pp. 1891-1900, Nov 2006.

[22] Y. Yang and S. R. Cherry, "Observations regarding scatter fraction and NEC measurements for small animal PET.," *IEEE Trans Nucl Sci,* vol. 53, pp. 127-132, 2006.

[23] S. Rechka, R. Fontaine, M. Rafecas, and R. Lecomte, "Development and validation of a GATE simulation model for the LabPET scanner.," *IEEE Trans Nucl Sci,* vol. 56, pp. 3672-3679, 2009.